



Decorating graphene oxide with zeolitic imidazolate framework (ZIF-8) and pseudo-boehmite offers ultra-high adsorption capacity of diclofenac in hospital effluents

Payam Arabkhani ^a, Hamedreza Javadian ^b, Arash Asfaram ^{c, **}, Mohamed Ateia ^{d, *}

^a Department of Chemistry, Tehran North Branch, Islamic Azad University, Tehran, Iran

^b Department of Chemical Engineering, ETSEIB, Universitat Politècnica de Catalunya, Diagonal 647, 08028, Barcelona, Spain

^c Medicinal Plants Research Center, Yasuj University of Medical Sciences, Yasuj, Iran

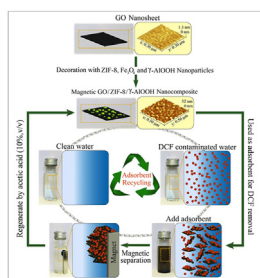
^d Department of Chemistry, Northwestern University, Evanston, IL, 60208, USA



HIGHLIGHTS

- Magnetic GO/ZIF-8/ γ -AlOOH-NC was synthesized for DCF removal from aqueous effluents.
- The reaction fitted pseudo-second-order kinetic model with an endothermic reaction.
- GO/ZIF-8/ γ -AlOOH-NC showed high adsorption capacity of 2594 mg g⁻¹ for DCF.

GRAPHICAL ABSTRACT



ARTICLE INFO

Article history:

Received 10 November 2020

Received in revised form

5 January 2021

Accepted 8 January 2021

Available online 11 January 2021

Handling Editor: Dr Y Yeomin Yoon

Keywords:

Graphene oxide

ZIF-8

Diclofenac sodium removal

Magnetic nanocomposite

Simulated hospital effluent

Ultra-high adsorption capacity

ABSTRACT

This study reports on an easy and scalable synthesis method of a novel magnetic nanocomposite (GO/ZIF-8/ γ -AlOOH) based on graphene oxide (GO) nanosheets decorated with zeolitic imidazolate framework-8 (ZIF-8), pseudo-boehmite (γ -AlOOH), and iron oxide (Fe₃O₄) nanoparticles by combining solvothermal and solid-state dispersion (SSD) methods. The nanocomposite was successfully applied to remove of diclofenac sodium (DCF) – a widely used pharmaceutical – from water. Response Surface Methodology (RSM) was used to optimize the adsorption process and assess the interactions among the influencing factors on DCF removal efficiency; including contact time, adsorbent dosage, initial pH, solution temperature, and DCF concentration. Adsorption isotherm results showed a good fitting with the Langmuir isotherm model with an exceptional adsorption capacity value of 2594 mg g⁻¹ at 30 °C, which was highly superior to the previously reported adsorbents. In addition, kinetic and thermodynamic investigations further illustrated that the adsorption process was fast (equilibrium time = 50 min) and endothermic. The regeneration of GO/ZIF-8/ γ -AlOOH nanocomposite using acetic acid solution (10% v/v) after a simple magnetic separation was confirmed in five consecutive cycles, which eliminate the usage of organic solvents. The nanocomposite has also shown a superior performance in treating a simulated hospital effluent that contained various pharmaceuticals as well as other organic, and inorganic constituents.

© 2021 Elsevier Ltd. All rights reserved.

* Corresponding author.

** Corresponding author.

E-mail addresses: arash.asfaram@yums.ac.ir (A. Asfaram), ateia@northwestern.edu (M. Ateia).

1. Introduction

Diclofenac sodium (DCF), a pharmacological compound with anti-inflammatory and analgesic properties, is used in enormous amounts worldwide (Huang et al., 2019). Even trace concentrations of DCF (as low as parts per million level) can cause aquatic ecotoxicity and risk for human health from hemodynamic changes (Xiong et al., 2019). DCF has been also detected frequently in drinking waters as a micropollutant owing to its high water solubility and polarity (Fan et al., 2019). This is therefore a major concern since DCF is not biodegradable, and conventional treatment methods fail to completely remove it from water (Wu et al., 2020). Thus, alternative treatment are still needed for efficient removal of DCF (Hiew et al., 2019a).

Adsorption-based techniques are desirable amongst the diverse chemical and biological methods for the treatment of contaminated water because of their high performance, economic viability, suitability over a wide concentration range, easiness to install, and low energy consumption (Liang et al., 2019). To remove pharmaceuticals from aqueous solutions, various kinds of adsorbents have been tested (e.g., activated carbon (Bhadra et al., 2016; Khalid et al., 2020), graphene oxide (Nam et al., 2015; Li et al., 2018), metal-organic framework UiO-66, and polyethylenimine modified composite microspheres (Fan et al., 2019; Ateia et al., 2018). Nevertheless, previously tested adsorbents had some drawbacks such as low adsorption capacity, pH dependency, and hard recyclability and low ability to separate adsorbents from solutions. Recently, nanocomposites have shown great application because of having high adsorption capacity (Xiong et al., 2019) generated from numerous surface adsorption sites, high capacity of sorption, and large number of functional groups compared to their precursor components (El-Maghrabi et al., 2017; Asfaram et al., 2020; Heu et al., 2020; Mousa et al., 2020).

To remove micropollutants from contaminated waters, graphene-based nanocomposites offer a great potential because of their delocalized π electrons, oxygen containing functional groups, and the abundance of active adsorption sites (Hiew et al., 2019a, 2019b). Thus, an efficient combination of graphene oxide nanosheets and other nanomaterials has been reported to produce nanocomposites for water treatment (Hiew et al., 2019b; Shi et al., 2020). In addition, zeolitic imidazolate framework (ZIFs), a subfamily of metal-organic frameworks, showed to have several exceptional properties, such as thermal stability and chemical robustness (Hasan et al., 2016). ZIFs are nanoporous and consist of organic linkers and metal centers, which have received increasing attention due to their unique physical characteristics such as large surface area, high volume of well-defined pores, and low density (Abdi et al., 2019). Among them, ZIF-8 is a tetrahedral framework synthesized by zinc ions and imidazolate ligands with sodalite that is applied as an efficient adsorbent for removing pollutants from water and presented great potential due to being highly stable, ultrahigh porous, and hydrophobic in nature (Jian et al., 2015).

This study aimed at the synthesis of a novel magnetic graphene-based nanocomposite (GO/ZIF-8/ γ -AlOOH) by combining solvothermal and solid-state dispersion (SSD) methods. In the synthesis process, graphene oxide nanosheets was used as the main component of the composite decorated with ZIF-8, γ -AlOOH, and superparamagnetic Fe_3O_4 nanoparticles. ZIF-8 has been chosen as a support to develop nanocomposites because of its outstanding chemical stability, a suitable structure for adsorption especially through π -interaction, and high porosity (Feng et al., 2016). Nano Fe_3O_4 gives the nanocomposite a magnetic property for easy

separation and recovery from solutions (Zheng et al., 2014). The nanocomposite also included γ -AlOOH nanoparticles due to being rich in OH-functional groups for better adsorption of targets containing H-bond. The nanocomposites and its precursor materials were thoroughly analyzed using X-ray powder diffraction (XRD), Fourier-transform infrared spectroscopy (FTIR), Field Emission Scanning Electron Microscopy with Energy Dispersive X-Ray Spectroscopy (FE-SEM-EDX), Atomic force microscopy (AFM), Vibrating-sample magnetometer (VSM), Brunauer–Emmett–Teller (BET), and Thermogravimetric analysis and differential gravimetric analysis (TGA/DTG) techniques. The nanocomposite was then introduced as a superior adsorbent for highly efficient DCF removal from aqueous effluents including simulated hospital wastewater. Response Surface Methodology with Central Composite Design (RSM-CCD) was used to assess the effects of operational parameters such as contact time, solution pH, adsorbent dosage, initial dye concentration, and water temperature on the adsorption capacity.

2. Materials and methods

2.1. Materials, chemicals, and instrumentation

All chemicals, reagents, and instruments applied in this research are fully described in the “Electronic Supplementary Information” file (Section S.2.1).

2.2. Materials synthesis

First, natural graphite was used to synthesis GO nanosheets using by the modified Hummers' method (Muzyka et al., 2017). ZIF-8 was synthesized in an aqueous system at room temperature (Kida et al., 2013). Also, the simple solvothermal method was applied to the synthesis of γ -AlOOH nanoparticles (Abdollahifar et al., 2018). The synthesis of Fe_3O_4 nanoparticles was done by an environmental-friendly sol-gel technique (Basith et al., 2016). Finally, the magnetic GO/ZIF-8/ γ -AlOOH-NC was obtained by combining the solvothermal and solid-state dispersion (SSD) method. For this purpose, 0.50 g of GO nanosheets was exfoliated by ultrasonication in 100 mL ethanol for more than 2 h. Subsequently, as-prepared ZIF-8 (30 %wt), Fe_3O_4 (10 %wt), and γ -AlOOH (30 %wt) nanoparticles were respectively added to the homogeneous GO suspension. The mixture was stirred by a glass muddler until the complete evaporation of ethanol, and then the as-prepared nanoparticles were immobilized on the surface of GO nanosheets by SSD method. The black precipitate was moved to a 250 mL Teflon-lined stainless-steel autoclave and kept at 200 °C for 12 h. In continue, it was naturally cooled to room temperature. By using an external magnetic field, the precipitate was collected, washed with deionized water several times and finally dried at 80 °C. Fig. 1 presents a schematic diagram of the synthesis process of magnetic GO/ZIF-8/ γ -AlOOH-NC, and each step was confirmed by 2-dimensional (2D) and 3-dimensional (3D) AFM images. As can be seen in Fig. 1, in the first stage, GO nanosheets were exfoliated well by ultrasonication. The smooth surfaces of GO nanosheets can be seen in 2D and 3D AFM images before decoration with the other prepared nanoparticles. In the following, the exfoliated GO nanosheets were decorated with ZIF-8, Fe_3O_4 , and γ -AlOOH nanoparticles, respectively. In addition, decorating the exfoliated GO nanosheets with ZIF-8, γ -AlOOH, and Fe_3O_4 nanoparticles might be accomplished through the H-bond, π - π interaction, and covalent bonding with GO nanosheets surface functional groups.

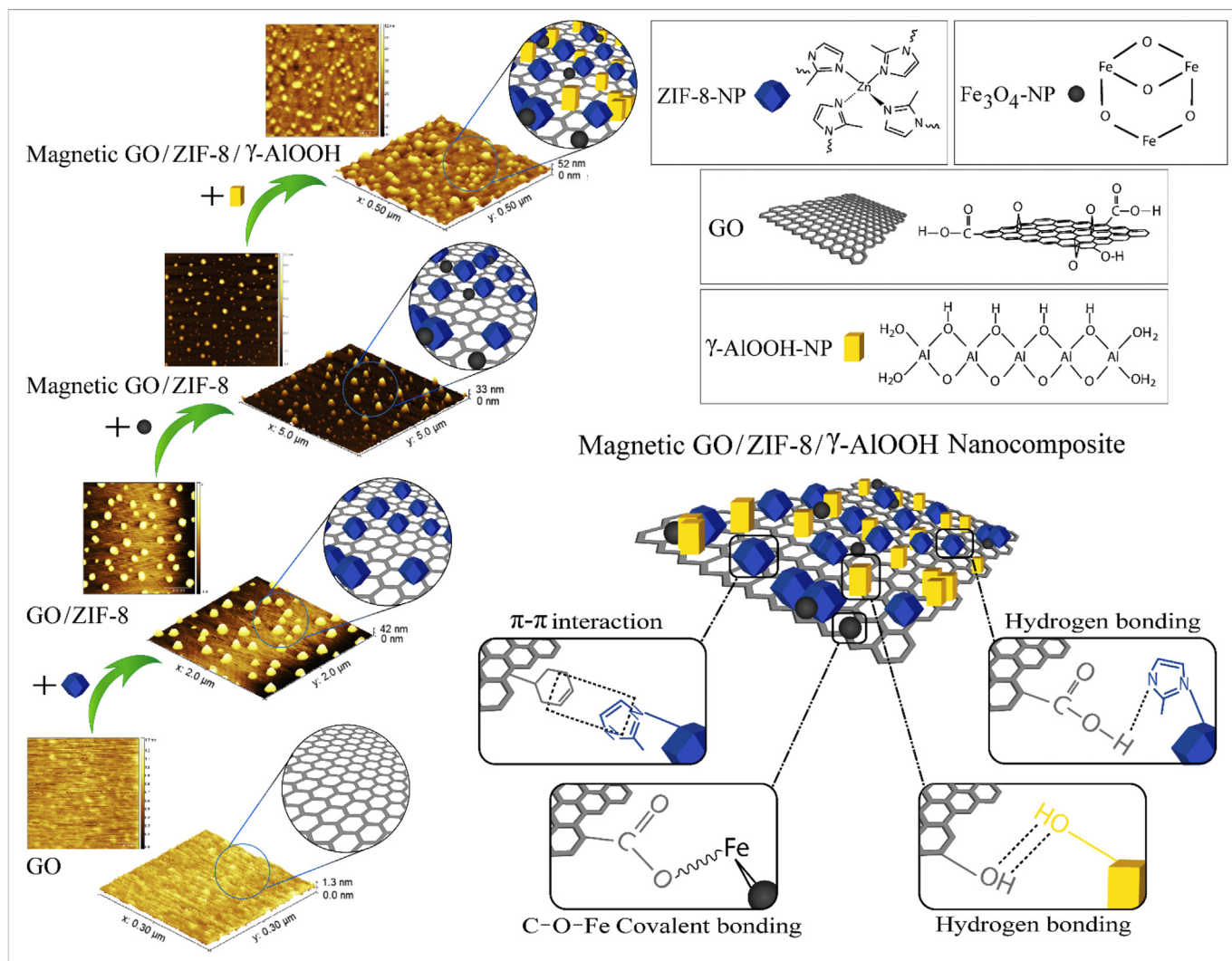


Fig. 1. Synthesis process of GO/ZIF-8/γ-AlOOH-NC.

2.3. Adsorption experiments

The experiments were accomplished by batch method to see the impact of the main parameters such as initial pH of solution (4–10), contact time (10–90 min), initial DCF concentration (30–150 mg L⁻¹), temperature (10–50 °C), and the nanocomposite mass (0.5–2.5 mg) on the performance of DCF adsorption and also obtain the data of kinetic and equilibrium. The pH of DCF solutions was adjusted by using 0.1 mol L⁻¹ HCl or/and NaOH solution. Adsorption experiments were performed by adding a specific amount of the adsorbent to a 250 mL Erlenmeyer flask containing 50 mL solution of DCF with a given concentration, and then a thermostatic orbital shaker was used to shake the mixture at 300 rpm. By using an external magnet, the adsorbent separation was carried out at the end of process. By using a double beam UV/Vis spectrophotometer after the treatment, the residual concentration of DCF was detected at the wavelength of 276 nm. Finally, the capacity of adsorption (q_t , mg g⁻¹) at time t , and the removal percentage (R %) of DCF were determined by equations used in the literature (Kunde et al., 2019; Yang et al., 2019; Ateia et al., 2020).

The interaction impact of various parameters was evaluated by CCD of RSM statistical design for the prediction of the response and optimization of DCF adsorption process (Khafri et al., 2017). To

model the response surface, thirty-two experiments proposed by a five-level CCD with six replicates at the center point were performed. DCF concentration (X_1), initial pH (X_2), adsorbent dose (X_3), temperature (X_4), and contact time (X_5) were used as the variables (independent factors), and the removal efficiency of DCF was considered as response (dependent factor). Table S1 presents the design of this study. STATISTICA software (version 10, StatSoft Inc., Tulsa, OK, USA) and analysis of variance (ANOVA) was applied to generate and analyze the data of the experiments. The generation of 2D contour plots and 3D curves of the response surfaces was accomplished using the same software.

2.4. Desorption and regeneration studies

The mechanism of adsorption can be elucidated by adsorption-desorption studies, and the regeneration of adsorbent helps to determine whether the adsorption process is economic or not. For this purpose, the solvents of ultrapure water, acetic acid (10% v/v), and methanol (10% v/v) were used as elution agents. For desorption of DCF, the eluents (50 mL) in the Erlenmeyer flasks containing the DCF-loaded nanocomposite were placed on a shaker. After attaining the equilibrium condition, an external magnetic field was used to separate the DCF-loaded nanocomposite. DCF concentration in

the solutions after desorption process was determined using UV–vis spectrophotometer after each desorption step. The DCF-loaded adsorbent was regenerated and reused in the subsequent adsorption experiments.

3. Results and discussion

3.1. Characterization of the synthesized materials

The synthesized materials were characterized by XRD for the confirmation of their crystal structure and purity of the as-synthesized samples, and the results are shown in Fig. 2. The pattern of XRD for GO nanosheets (Fig. 2a) exhibits a main characteristic diffraction peak at 10.8° , corresponding to the diffraction peak (001) of GO structure (El-Maghrabi et al., 2017; Boruah and Das, 2020). Moreover, two additional peaks were detected at 27.80° (002) and 42.44° (101) that correspond to the unoxidized natural graphite (Zhang et al., 2011; Accocella et al., 2015). The pattern of XRD for ZIF-8 nanoparticles is indicated in Fig. 2b. The sharp diffraction peaks show the particles with highly crystalline structure. The diffraction peaks appeared at 7.3° (011), 10.3° (002), 12.7° (112), 14.7° (022), 16.4° (013), 18.0° (222), and 24.6° (233) are in good agreement with pure ZIF-8 structure in other previous reports (Jian et al., 2015). The XRD pattern of magnetic Fe_3O_4 nanoparticles is shown in Fig. 2c. The diffraction peaks appeared at 30.24° (220), 35.53° (311), 43.14° (400), 53.57° (422) and 57.08° (511) could be related to the cubic spinel phase of Fe_3O_4

nanoparticles (JCPDS 88–0866). Fig. 2d shows the XRD pattern of γ - AlOOH nanoparticles. The diffraction peaks appeared at 7.3° (011), 10.3° (002), 12.7° (112), 14.7° (022), 16.4° (013), 18.0° (222), 24.6° (233), and 26.7° (134) agree well with the pure γ - AlOOH standard card (JCPDS No. 4–802), and no obvious XRD peaks are seen from other phases of alumina. The XRD pattern of magnetic GO/ZIF-8/ γ - AlOOH -NC is presented in Fig. 2e. As can be seen, the well-defined peaks reveal the high crystallinity of the nanocomposite. In addition, the diffraction peaks of ZIF-8, Fe_3O_4 , and γ - AlOOH nanoparticles can be clearly indexed in the XRD pattern of the nanocomposite that confirm their existence in magnetic GO/ZIF-8/ γ - AlOOH -NC. It is worth noting that the d001 peak of GO nanosheets is not observed in the XRD pattern of magnetic GO/ZIF-8/ γ - AlOOH -NC because GO nanosheets are highly exfoliated and dispersed during the synthesis of the nanocomposite (Jabbari et al., 2016b). The well appearance of the highly intense peak of ZIF-8 in the XRD pattern of magnetic GO/ZIF-8/ γ - AlOOH -NC attributes to the high concentration of ZIF-8 crystals (30 %wt) in the nanocomposite structure. In addition, Fe_3O_4 peaks in the XRD pattern of magnetic GO/ZIF-8/ γ - AlOOH -NC has lower intensity compared with pure Fe_3O_4 nanoparticles, which could be related to the low concentration of Fe_3O_4 in the nanocomposite.

The FT-IR spectra of the synthesized samples are shown in Fig. 3. The characteristic peaks of GO nanosheets (Fig. 3a) are at

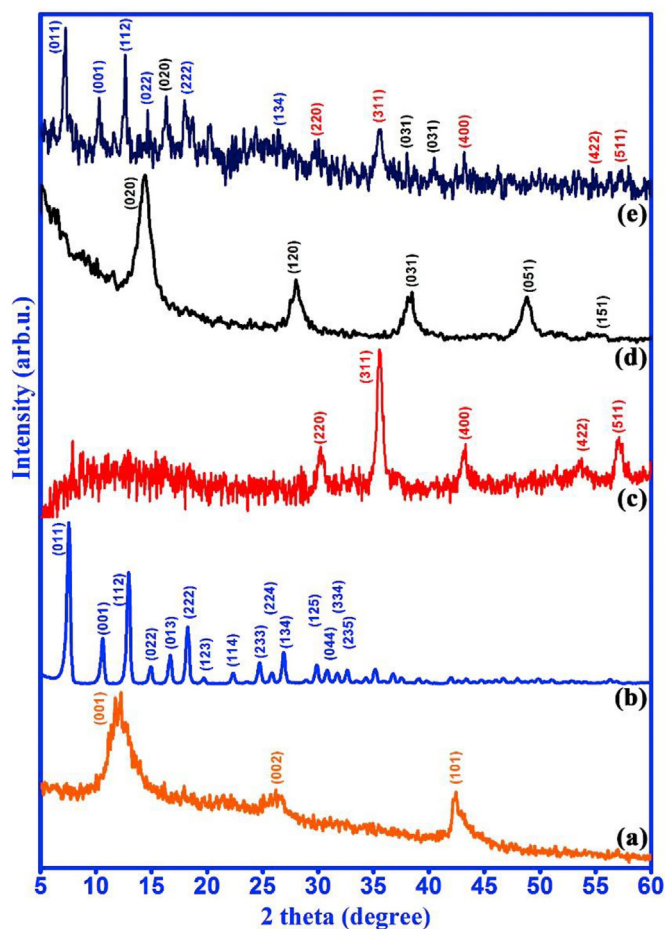


Fig. 2. XRD patterns of (a) GO, (b) ZIF-8, (c) Fe_3O_4 , (d) γ - AlOOH , and (e) magnetic GO/ZIF-8/ γ - AlOOH -NC.

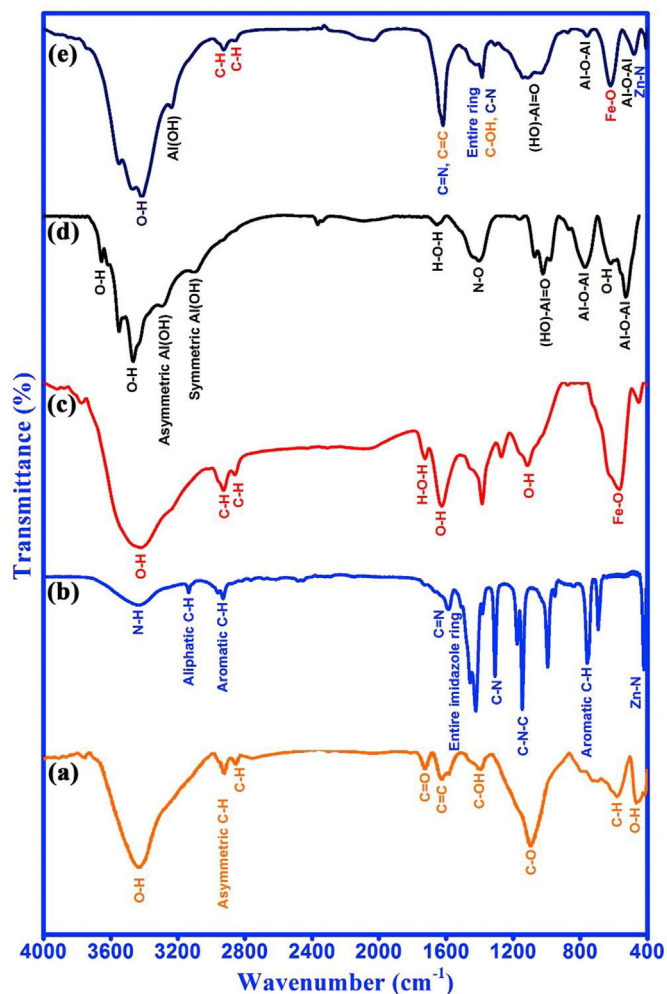


Fig. 3. FT-IR spectra of (a) GO, (b) ZIF-8, (c) Fe_3O_4 , (d) γ - AlOOH , and (e) magnetic GO/ZIF-8/ γ - AlOOH -NC.

3432 cm^{-1} (O–H stretching vibration), 2924 cm^{-1} and 2854 cm^{-1} (C–H stretching vibration), 1712 cm^{-1} (C=O stretching vibration of –COOH), 1627 cm^{-1} (C=C stretching vibration of aromatic rings), 1390 cm^{-1} (C–OH stretching vibration), 1094 cm^{-1} (C–O stretching vibration of C–O–C groups), 568 cm^{-1} (C–H out of plane bending vibration), and 464 cm^{-1} (O–H out of plane bending vibration). In the case of ZIF-8 nanoparticles (Fig. 3b), Zn–OH groups and physically adsorbed water are located at 3500 cm^{-1} (Tanaka and Miyashita, 2017). The aliphatic and aromatic C–H stretch of imidazole are respectively at 3135 and 2929 cm^{-1} (Liu et al., 2016). The bending of aromatic sp^2 C–H is shown with the peaks of 760 and 690 cm^{-1} (Kaur et al., 2017). The strong band observed at 421 cm^{-1} relates to the stretching of Zn–N due to the connection of the zinc atoms in the structure of ZIF-8 to N atoms of 2-Melm linker during ZIF-8 formation. For Fe_3O_4 nanoparticles (Fig. 3c), the characteristic peak at 566 cm^{-1} can be attributed to the Fe–O bond. The existence of the Fe–O bond authenticates the magnetite property of Fe_3O_4 nanoparticles (Kaur et al., 2019). The characteristic peaks at 1115 and 1624 cm^{-1} can be attributed to the deformation of OH band of the bulk OH groups. The peak at 3412 cm^{-1} is the OH stretching vibration of $\text{Fe}(\text{OH})_2$, $\text{Fe}(\text{OH})_3$ and FeOOH formed from hydrolyzation on the surface of Fe_3O_4 (Lu et al., 2010). For γ -AlOOH (Fig. 3d), the peaks located at 3295 and 3095 cm^{-1} are respectively related to the asymmetric and symmetric stretching of the inter-layer OH groups. The adsorbed water shows O–H bending modes at 1622 cm^{-1} . Nitrate anion shows the stretching of N–O at 1389 cm^{-1} due to incomplete removal by washing; therefore, a more intense of this band is seen for the samples with the existence of nitrate anion (Abdollahifar et al., 2018). The asymmetric stretching of (HO)–Al=O is seen at approximately 1076 and 1152 cm^{-1} (Zhang et al., 2016). The bending and stretching of AlO_6 are respectively detected at 522 and 724 cm^{-1} (Choi et al., 2018). As for FT-IR spectrum of magnetic GO/ZIF-8/ γ -AlOOH-NC (Fig. 3e), the peaks related to the blank materials are appeared well in the spectrum. This result confirms the accurate and successful decoration of GO nanosheets with ZIF-8, Fe_3O_4 , and γ -AlOOH nanoparticles, which in agreement with the XRD result (Jabbari et al., 2016a).

The surface roughness and topography of synthesized blank GO nanosheet and magnetic GO/ZIF-8/ γ -AlOOH-NC are shown by the 2D and 3D AFM images with the corresponding height profiles in Fig. 4a and b. According to the AFM, GO nanosheets (Fig. 4a) include a flat surface successfully exfoliated by sonication, which is in accordance with the XRD result. No structures other than GO were found. The height profile of the AFM shows 1.3 nm of thickness for the sheets of GO, which matches the typical thickness of monolayer GO sheets (Mahmoudi et al., 2012). The AFM images of magnetic GO/ZIF-8/ γ -AlOOH-NC are shown in Fig. 4c and d. The nanomaterials are uniformly distributed throughout the GO surface, and the vertical profile shows thickness for the nanocomposite of 52 nm. The flat surface of GO became rough with the existence the nanomaterials that would enhance the specific surface area and increase adsorption active sites of the nanocomposite (Habibi, 2014).

The sizes and surface morphologies of blank GO nanosheets and magnetic GO/ZIF-8/ γ -AlOOH-NC were studied by FE-SEM images. The EDX analysis were also carried out to further investigate the elemental composition and distribution of elements (Fig. 5). The FE-SEM image of GO nanosheets (Fig. 5a) shows a lamellar sheet-like structure and smooth surfaces with the sizes of around 10 μm . Fig. 5b shows the elemental mapping of GO nanosheets, and the distribution of C and O on GO nanosheets surface can be seen observably. The weight percentages of C and O in GO nanosheets determined by EDX spectrum analysis are shown in Fig. 5d. Fig. 5e shows the FE-SEM image of magnetic GO/ZIF-8/ γ -AlOOH-NC, in which the easily observable lamellar sheets of GO indicate the

presence of GO layers in the nanocomposite structure. Additionally, it can be seen that GO nanosheets is well decorated and partially covered by the nanomaterials, and an adequate interfacial contact is developed between the nanoparticles and GO nanosheets that can lead to the favorable stability of the nanocomposite. The elemental mapping and weight percentages of the synthesized nanocomposite are shown in Fig. 5c and f, respectively. As can be seen, the nanocomposite is composed of C, O, Al, Zn, N, and Fe elements. The elements of C, Al, Zn and N, and Fe in the nanocomposite respectively relate to GO nanosheets, and γ -AlOOH, ZIF-8, and Fe_3O_4 nanoparticles, which confirm the successful decoration of GO nanosheets by γ -AlOOH, ZIF-8, and Fe_3O_4 nanoparticles. The low content of Fe element in the nanocomposite can also be seen clearly. This observation is in complete agreement with the findings from the XRD and FT-IR results.

Adsorption capacity can be affected by textural characteristics particularly the specific surface area that is determined from the measurements of nitrogen physisorption. Fig. 6 shows the isotherms of nitrogen adsorption-desorption and BJH pore-size distributions for the synthesized materials, and the results of textural characteristics are presented in Table S2. Based on the classification of IUPAC, GO nanosheets show an isotherm of typical type III with the hysteresis loop of type H3 obtained from the macroporous or non-porous solid and lamellar aggregate structure (Yang et al., 2018). An adsorption isotherm of typical type IV with the hysteresis loop of type H3 is shown for Fe_3O_4 nanoparticles. This isotherm type is usually related to mesoporous materials with slit shaped pores (Bohström and Lillerud, 2018). γ -AlOOH nanoparticles show an isotherm of typical type IV with the hysteresis loop of type H1, which confirm the presence of agglomerates mesoporous materials that have a narrow pore size distribution. The isotherm of ZIF-8 is between type I and type IV with hysteresis loop of type H4. This obviously suggests the existence of microporous and a certain amount of small mesoporous in ZIF-8. Type H4 hysteresis loop is associated with narrow slit-like pores. Interestingly, the adsorption isotherm of magnetic GO/ZIF-8/ γ -AlOOH-NC shows a typical adsorption isotherm of type I with the hysteresis loop of type H4 that is related to a material with microporous and small mesoporous characteristics containing narrow slit-like pores, where the formations of mono- and then multi-layer are taken place on the surface (Cychosz et al., 2017). In addition, magnetic GO/ZIF-8/ γ -AlOOH-NC shows a higher specific surface area than other materials that may be owing to the effective dispersion of the nanoparticles onto GO layers, causing the formation of the micro mesoporous structure and the addition of ZIF-8 nanoparticles with a high specific surface area.

The thermal degradation and stability of the samples were investigated using TGA/DTG methods, and the results are shown in Figure S1. A careful observation of magnetic GO/ZIF-8/ γ -AlOOH-NC TGA and DTG curves (Figures S1e and S1f) suggests that magnetic GO/ZIF-8/ γ -AlOOH-NC has a multi-step decomposition. As illustrated in Figures S1e and S1f, the first degradation step from 25 to 180 $^{\circ}\text{C}$ (8.74%) with T_{max} peak at 149.64 $^{\circ}\text{C}$ is related to water evaporation and the molecules of methanol or Hmim. The second degradation step from 180 to 370 $^{\circ}\text{C}$ (10.55%) with T_{max} peak at 267.06 $^{\circ}\text{C}$ corresponds to the oxygen-containing functional groups pyrolysis of GO nanosheets and water loss from γ -AlOOH hydroxyl groups. The range of 370–580 $^{\circ}\text{C}$ (13.38%) with T_{max} peak at 509.21 $^{\circ}\text{C}$ is the third step of degradation attributed to the molecules decomposition of organic linker in the structure of ZIF-8. The fourth degradation step from 580 to 800 $^{\circ}\text{C}$ (21.21%) with T_{max} peak at 711.17 $^{\circ}\text{C}$ relates to the carbon skeleton combustion of GO nanosheets and synthesized ZIF-8, γ -AlOOH, and Fe_3O_4 thermal decomposition. It should be noted that the nanocomposite does not

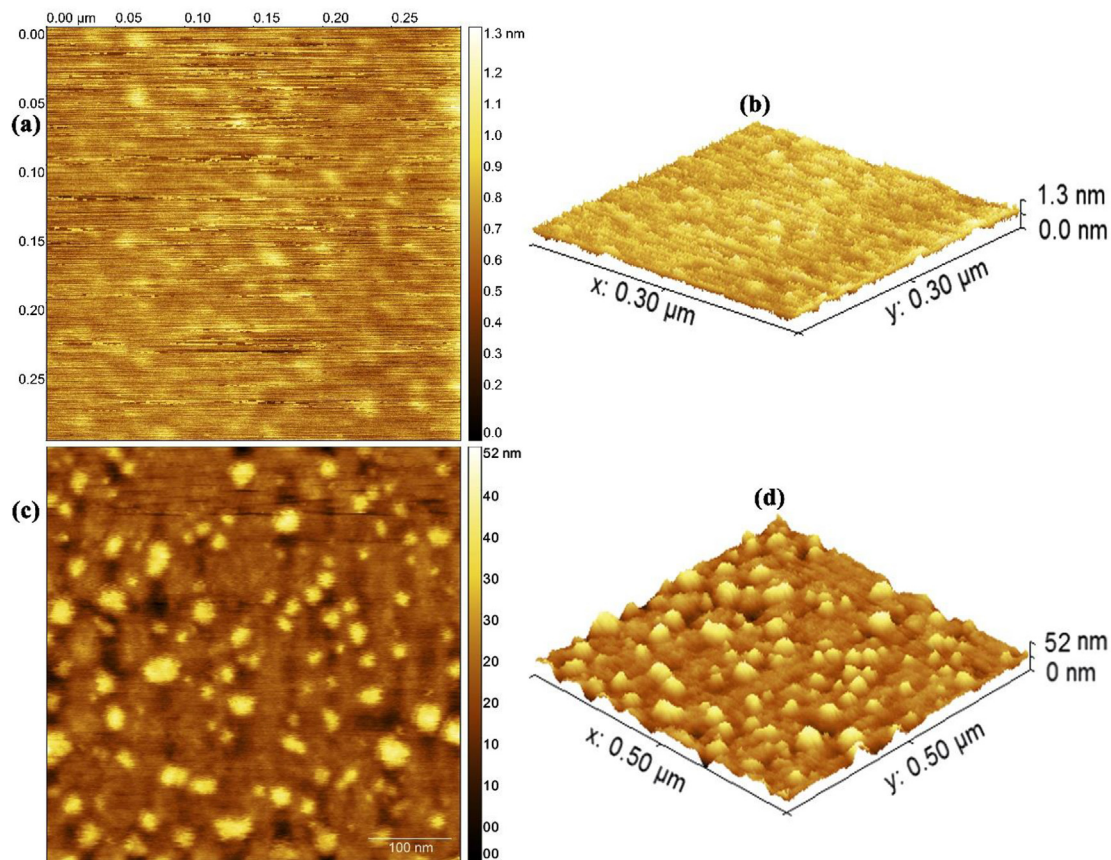


Fig. 4. (a) 2D, and (b) 3D AFM images of GO, (c) 2D, and (d) 3D AFM images of magnetic GO/ZIF-8/γ-AIOOH-NC.

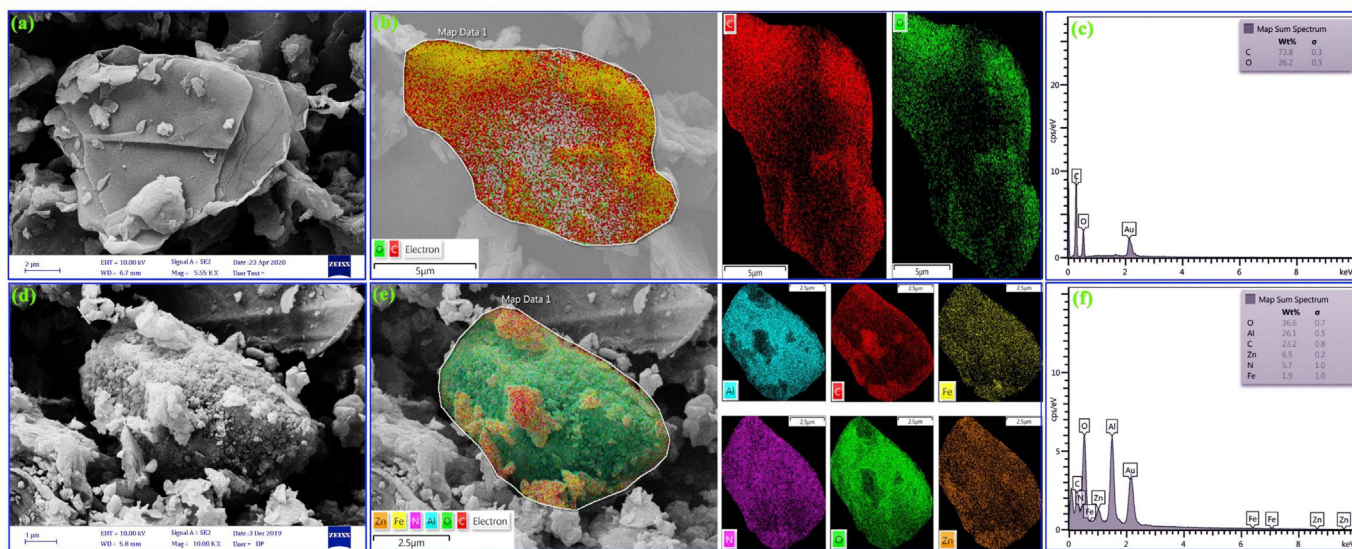


Fig. 5. (a) FE-SEM image, (b) EDX mapping and (c) EDX analysis of GO and (d) FE-SEM image, (e) EDX mapping, and (f) EDX analysis of magnetic GO/ZIF-8/γ-AIOOH-NC.

exhibit greater thermal stability than the blank materials that is likely due to this fact that the nanocomposite is not mostly synthesized through strong chemical bonds like covalent bond between the blank materials during the synthesis process. However, the total loss in weight from the temperature of room to 800 °C is around 54%. These results suggest that the synthesized

nanocomposite possesses a good thermal stability. These TGA/DTG results of the materials with the main degradation characteristics are summarized in Table 1 (Jabbari et al., 2016b; Ateia et al., 2017a).

Figure S2 shows the curves of typical magnetization measured by VSM technique at the temperature of room for blank Fe₃O₄ nanoparticles and magnetic GO/ZIF-8/γ-AIOOH-NC. As indicated in

the figure, the loops of both samples exhibit very low coercive field and remanence values, which indicate that the samples approximately behave as superparamagnets at room temperature (Yu et al., 2015). The saturation magnetization (M_s) of blank Fe_3O_4 nanoparticles and magnetic GO/ZIF-8/ γ -AIOOH-NC were determined to be 57.32 eum g^{-1} and 9.75 eum g^{-1} , respectively. The lower saturation magnetization value of the nanocomposite compared with blank Fe_3O_4 nanoparticles could be corresponded to the relatively low mass ratio of Fe_3O_4 nanoparticle loaded on magnetic GO/ZIF-8/ γ -AIOOH-NC, which was confirmed by the EDX result. In spite of this reduction in the saturation magnetization value, it is enough to certify the easy separation of magnetic GO/ZIF-8/ γ -AIOOH-NC by a small external magnet and make the solid-liquid phase separation to be easy and effective (Lu et al., 2017; Xie and Huang, 2018).

3.2. Central composite design (CCD)

To model the removal process of DCF, a quadratic model was chosen proposed by the software. The results were 33.5 and 99.9% for the minimum and maximum adsorption of DCF, respectively. The equation obtained by removing the insignificant terms from the proposed model was given as follows:

$$R\%_{DCF} = -153.7 - 0.48X_1 + 39.18X_2 + 25.05X_3 + 2.96X_4 + 2.62X_5 + 0.04X_1X_2 + 0.01X_1X_5 + 2.2X_2X_3 - 0.17X_2X_4 - 0.08X_2X_5 + 0.34X_3X_4 - 0.15X_3X_5 - 0.02X_4X_5 - 0.004X_1^2 - 2.7X_2^2 - 11.11X_3^2 - 0.02X_4^2 - 0.02X_5^2 \quad (1)$$

The synergistic and antagonistic effects in Eq. (1) are indicated by positive and negative signs of the coefficients. It shows the negative impact of initial DCF concentration on DCF removal, while pH, contact time, temperature, and magnetic GO/ZIF-8/ γ -AIOOH-NC mass affect positively.

To validate the model for DCF adsorption and determine the significance of the individual and the interactive variables, ANOVA was used as an important criterion. A favorable result is shown by the low and high values of p-values (<0.05) and F-values, respectively (Ghaedi et al., 2015). As can be seen from Table S3, the significance of the model is confirmed by the very low p-value (<0.0001) and high F-value (65.92). A p-value less than 0.05 for all linear terms, interactions (X_1X_2 , X_1X_5 , X_2X_3 , X_2X_4 , X_2X_5 , X_3X_4 , X_4X_5), as well as quadratic terms shows them as effective terms in the predicted model. The values of R^2 and adjusted R^2 were obtained to be respectively 0.9917 and 0.9767, explaining 99.17% validity for the response values by the predicted model.

Solution pH as an important physico-chemical parameter can affect on the properties of adsorbent surface and chemical structure of adsorbate. To understand better the initial pH effect on the adsorption performance, the pH of zero-point charge (pH_{zpc}) of the nanocomposite was studied. Fig. 7a shows the zeta potential of the nanocomposite measured at initial pH ranging from 2 to 10, and the pH_{zpc} of the nanocomposite is 7.1. The nanocomposite surface charge at pH below 7.1 is positive, and its surface charge is negative at pH beyond 7.1. On the other hand, the acid dissociation constant value (pK_a) of DCF is approximately 4.2, meaning that DCF is cationic at $pH < 4.2$ and anionic at $pH > 4.2$. When the pH value of solution is < 4.2 , an electrostatic repulsion occurs between the positively charged nanocomposite and positively charged DCF molecules that is not favorable for adsorption process. At the pH of

4.2–7.1, the surface of the nanocomposite is positive, and DCF is anionic, consequently, the adsorption of DCF increases due to the strong electrostatic attraction between the nanocomposite and DCF molecules. At pH values beyond 7.1, the occurrence of electrostatic repulsion between the negatively charged nanocomposite and negatively charged DCF causes a decrease in the adsorption of DCF. It can be concluded from the results that the dominant mechanism for the adsorption process is electrostatic attraction, and other mechanisms can occur along with the electrostatic attraction.

To obtain a maximum removal of DCF, each factor was optimized. Fig. 7b and c shows the response surface plots for the DCF removal with the input parameters of pH, contact time, DCF concentration, adsorbent mass, and temperature.

As illustrated in Fig. 7b, DCF removal efficiency decreases with an increase in initial concentration ranging from 80 to 150 mg L^{-1} at pH value of 7.5. When DCF initial concentration is low in the solution, the quantity of active adsorption sites is high, consequently, high amount of DCF can be easily adsorbed. On the contrary, at high initial concentration, a decrease is seen at higher DCF initial concentration since the total adsorption active sites are limited, resulting a decrease in removal percentage of DCF as expected.

The 3D response surface and contour plots for the interaction effects of the adsorbent mass-contact time and adsorbent mass-

temperature can be respectively seen in Fig.7c and d. The percentage removal of DCF increases from around 40 to 95% using 0.5 and 2.0 mg of magnetic GO/ZIF-8/ γ -AIOOH-NC, respectively (Fig. 7c). Increasing the adsorption of DCF with an increase in adsorbent mass can be corresponded to the increase in magnetic GO/ZIF-8/ γ -AIOOH-NC surface area and availability of more active adsorption sites. In addition, the adsorption efficiency of DCF becomes more by any increase in contact time and the adsorption of maximum DCF takes place within 50 min. A rapid adsorption is seen within 10 min owing to the high available active functional sites, and then a gradual occupation of the pores and surface active functional sites of magnetic GO/ZIF-8/ γ -AIOOH-NC to reach maximum removal percentage. Any increase in contact time up to 90 min results almost the same removal percentage as 50 min.

Fig. 7d illustrates increasing DCF adsorption with temperature increase, which indicates that the process of adsorption is endothermic. This result may be owing to an increase in DCF mobility with raising temperature, causing an increase in interaction between DCF molecules and the active sites available on the surface of the nanocomposite.

The optimum conditions (Figure S3) for DCF adsorption (99.29%) were found to be 2 mg of magnetic GO/ZIF-8/ γ -AIOOH-NC, initial DCF concentration of 80 mg L^{-1} , pH value of 7.5, contact time of 50 min, and temperature of $30 \text{ }^\circ\text{C}$. To validate the optimum conditions achieved by CCD, the experiments were carried out at the optimum conditions. The results showed an average error percentage <2.5%, revealing clearly that the proposed model for the adsorption of DCF is in good correspondence with the experimental results.

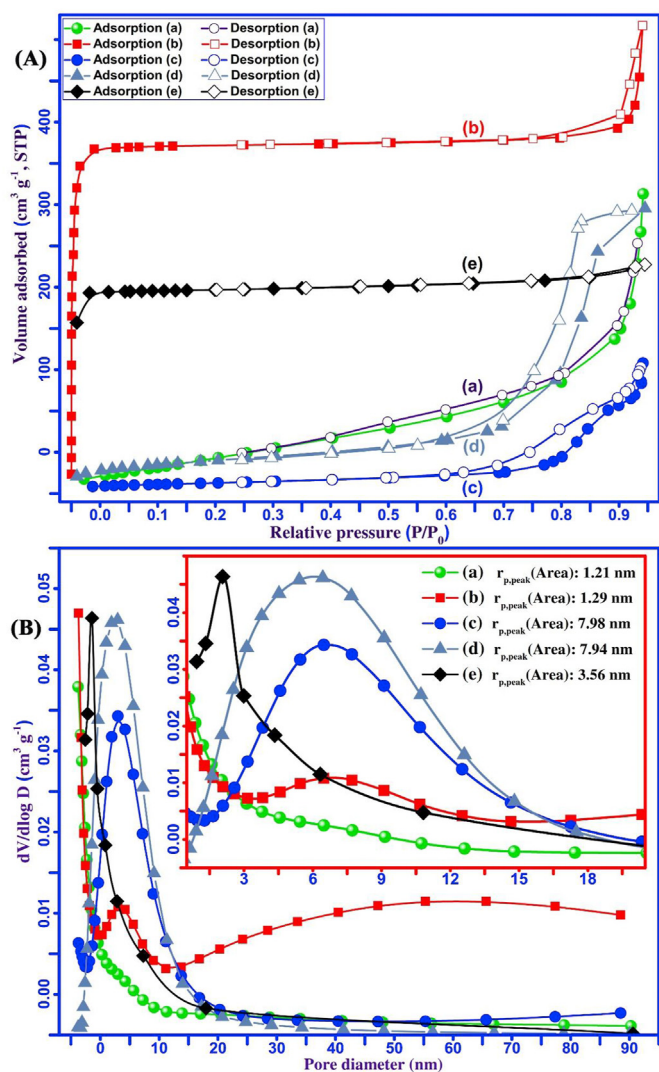


Fig. 6. Nitrogen adsorption/desorption isotherms and BJH pore size distribution of (a) GO, (b) ZIF-8, (c) Fe₃O₄, (d) γ-AlOOH, and (e) magnetic GO/ZIF-8/γ-AlOOH-NC.

Table 1
Data derived from thermal curves (TGA and DTG) of the materials.

Sample	Step	TGA Range (°C)	DTG max (°C)	Weight Loss (%)	Total Weight Loss (%)	Residue after 800 °C	Assignment
GO	1st	25–150	89.83	10.02	40.56	59.44	Evaporation of adsorbed H ₂ O molecules (Alam et al., 2017)
	2nd	150–400	228.4	22.05			Pyrolysis of oxygen-containing functional groups (Alam et al., 2017)
	3rd	400–800	579.26	8.49			Combustion of the carbon skeleton (Alam et al., 2017)
ZIF-8	1st	25–380	362.14	3.12	39.96	60.04	Removal of water and guest molecules (methanol or Hmim) and/or CO ₂ (Schejn et al., 2014)
	2nd	380–625	578.95	18.12			Decomposition of organic linker molecules, collapse of ZIF-8 structure and formed ZnO (Schejn et al., 2014)
Fe ₃ O ₄	3rd	625–800	682.16	18.72			Thermal decomposition of ZnO (Schejn et al., 2014)
	1st	25–200	46.0	1.02	9.98	90.02	Evaporation of adsorbed H ₂ O molecules (Ghorbani-Choghamarani et al., 2016)
γ-AlOOH	2nd	200–800	262.2	8.96			Dehydration of the surface OH groups (Wang et al., 2012)
	1st	25–200	34.57	3.83	41.48	58.52	Evaporation of adsorbed H ₂ O molecules (Ghorbani-Choghamarani et al., 2016)
Magnetic GO/ZIF-8/γ-AlOOH-NC	2nd	200–500	273.16	33.53			Water loss from structural hydroxyl groups (Ghorbani-Choghamarani et al., 2016)
	3rd	500–800	579.76	4.12			Boehmite decomposition to produce γ-alumina (γ-Al ₂ O ₃) (Kim et al., 2007)
	1st	25–180	149.64	8.74	53.88	46.12	Evaporation of adsorbed H ₂ O molecules and also guest molecules (methanol or Hmim)
	2nd	180–370	267.06	10.55			Pyrolysis of GO oxygen-containing functional groups and water loss from γ-AlOOH structural hydroxyl groups
	3rd	370–580	509.21	13.38			Decomposition of organic linker molecules, collapse of ZIF-8 structure
	4th	580–800	711.17	21.21			Combustion of the carbon skeleton of GO, thermal decomposition of produced ZnO, γ-AlOOH and Fe ₃ O ₄ nanoparticles.

3.3. Adsorption isotherm studies

The interaction between DCF and the adsorbent and the efficiency of the adsorbent for the adsorption of DCF can be studied by adsorption isotherms. Therefore, the adsorption data were fitted using various adsorption isotherm models including Langmuir (Langmuir, 1918), Freundlich (LeVan and Vermeulen, 1981), Temkin (Wawrzekiewicz and Hubicki, 2009), and Dubinin–Radushkevich (D-R) (Dubinin and Serpinsky, 1981) for the description of DCF adsorption process onto the nanocomposite. To fit a multi-layer adsorption onto a heterogeneous surface, Freundlich model is utilized, while Langmuir model is used to describe a monolayer adsorption of a target by the specific homogeneous sites of adsorbent. To investigate heterogeneous surface energy (sorption heat distribution non-uniformly), Temkin isotherm is used, in which the energy of adsorption related to the coverage of surface is used to express the interaction between adsorbate and adsorbent. Another isotherm model is Dubinin–Radushkevich that predicts adsorption process to be physically or chemically.

The results obtained from fitting the DCF adsorption data with the mentioned models are shown in Figure S4, and the parameters are given in Table S4. According to the coefficient of determination (R²) values, Langmuir model (0.999) better fits with the experimental data than Freundlich (0.743), Temkin (0.930), and D-R (0.960) models. This suggests that DCF adsorption is monolayer that occurs on a homogeneous surface of the nanocomposite. The maximum monolayer adsorption capacity of DCF by nanocomposite was 2594.3 mg g⁻¹, which was much greater than those of its constituent raw materials as well as other reported adsorbents in Table 2 that makes it to be greatly efficient for DCF removal from aqueous solution. The high adsorption capacity of nanocomposite for DCF may be due to the high surface area and the high presence of the surface functional groups in the mesopores region. The value of dimensionless constant (R_L) is a critical parameter that is used to study the applicability of Langmuir adsorption isotherm. The calculated R_L values are <1 (0.007–0.167), hence the adsorption process is favorable. n in Freundlich isotherm model reflects the heterogeneity factor and the adsorption intensity. The value of n is between 1 and 10, demonstrating a favorable adsorption (Saini et al., 2018). The value of E factor in the D-R isotherm model is 2.61 kJ mol⁻¹. When E value is below 8 kJ mol⁻¹, the process of

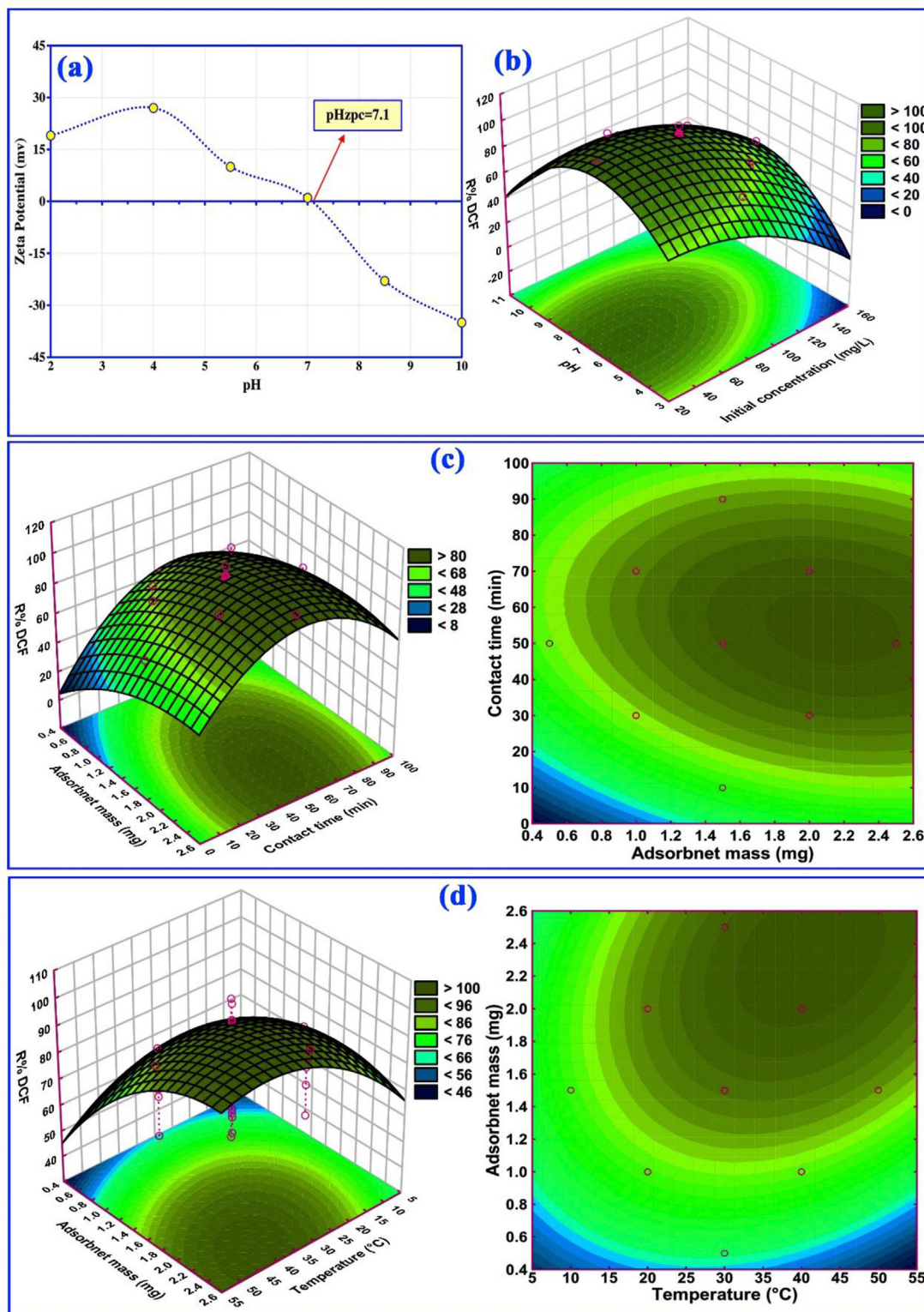


Fig. 7. (a) zeta potential of magnetic GO/ZIF-8/ γ -AlOOH-NC as a function of pH at 25 $^{\circ}C$ and three dimensional response surface plots of interactions and related counter plots for DCF adsorption: combined effect of pH and initial concentration (b), adsorbent mass-contact time (c) and adsorbent mass-temperature (d).

adsorption can be taken place physically (Singha and Das, 2013).

3.4. Adsorption kinetic models

Adsorption kinetics contain important information about solute

uptake rate at the interface of solid-solution and provide beneficial details corresponding to the pathways and mechanisms of reaction. Pseudo-first-order (Wong et al., 2004), pseudo-second-order (Ho, 2006), Elovich (Aksakal and Uzun, 2010), and intra-particle diffusion (Weber and Morris, 1963) models were used to analyze the

Table 2
Maximum adsorption capacity of DCF using different adsorbents at optimum condition*.

Adsorbent	Q_{max} (mg g ⁻¹)	Equilibrium Time (min)	Optimum pH	Ref
Graphene	59.67	200	10.0	Jauris et al. (2016)
Graphene oxide	653.9	15	6.0	Hiew et al. (2019b)
3D graphene aerogel	596.7	120	6.0	Hiew et al. (2019a)
Zeolitic imidazole framework functionalized with cetyltrimethylammonium bromide	60.60	90	5–10	Andrew Lin et al. (2015)
Fe ₃ O ₄ @MOF-100(Fe) magnetic microspheres	377.4	150	7.0	Zheng et al. (2018)
Metal-organic framework-derived porous carbon	320.0	720	>4.9	Bhadra et al. (2017)
Bilayer amino-functionalized cellulose nanocrystals/chitosan composite	444.4	50	4.5	Hu et al. (2019)
Mg/Al layered double hydroxide-Poly(m-Phenylenediamine) (LDH-PmPD) composite	521.0	720	2.0	Xiong et al. (2019a)
Polyethylenimine-functionalized sodium alginate/cellulose nanocrystal/polyvinyl alcohol	418.4	50	4.5	Fan et al. (2019)
Zr-based MOF (18%SO ₃ H-UiO-66)	263.0	1440	5.4	Hasan et al. (2016)
Natural zeolite modified with cetylpyridinium chloride	160.0	60	7.4	Krajišnik et al. (2011)
Magnetic amine-functionalized chitosan	469.5	60	4.5	Liang et al. (2019)
Fe ₃ O ₄ -NPs	35.0	50	7.5	This work*
γ-AIOOH-NPs	321.6	50	7.5	
GO-nanosheets	589.4	50	7.5	
ZIF-8-NPs	843.2	50	7.5	
Magnetic GO/ZIF-8/γ-AIOOH-NC	2594.3	50	7.5	

kinetic adsorption of DCF onto the nanocomposite.

The kinetic curves of DCF adsorption onto the nanocomposite are shown in Figure S5, and Table S5 presents the parameters of fitting the adsorption data with the models. As given in Table S5, second-order-model proposes a higher value of R^2 (0.9912) than other models; thus, it is more suitable for the kinetic data simulation. Moreover, the values of q_e obtained by using pseudo-second-order model is 2302.6 mg g⁻¹, which is more similar to that of the experiments (1937.5 mg g⁻¹). These results show the chemisorption of DCF onto the nanocomposite, which is faster at a higher temperature.

3.5. Adsorption thermodynamic

The parameters of thermodynamic, i.e. the changes in Gibbs free energy (ΔG°), enthalpy (ΔH°) and entropy (ΔS°), for the adsorption of DCF, were calculated using the formula reported in the previous publication (Arabkhani and Asfaram, 2020). The determination of ΔH° and ΔS° values was based on using the slope and intercept obtained from $\ln(K_e)$ versus $1/T$ plot, and their values are presented in Table S6. As can be seen in Table S6, the positive value of ΔH° (97.63 kJ mol⁻¹) proposes an endothermic adsorption process, revealing energy consumption for the reaction and increase in DCF adsorption by raising temperature. In addition, the value of $\Delta H^\circ > 40$ kJ mol⁻¹ means that the mechanism of DCF removal is chemisorption. During the adsorption of DCF, randomness at solid/liquid interface is suggested to be increased by the positive value of ΔS° (381.61 kJ mol⁻¹). The positive value of ΔS° also suggests the existence of an affinity between the nanocomposite and DCF that might be the electrostatic attraction as discussed above. The values of ΔG° are negative that express the spontaneity of DCF adsorption process. The values of ΔG° also suggest an increase in the reaction rate and subsequently adsorption performance of DCF due to decrease in ΔG° value at higher temperatures.

3.6. Regeneration and reusability studies

For an adsorption process to be economic, the regeneration of adsorbent and subsequently its reuse are as important issues that should be evaluated. In this research, after performing the adsorption of DCF, the nanocomposite was washed by three types of eluents including ultrapure water, acetic acid (10% v/v), and methanol (10% v/v) to investigate their ability for desorption of DCF. As shown in Fig. 8a, the ultrapure water acted as the least effective (51.7%) and acetic acid (10% v/v) as the most effective (98.2%) eluent

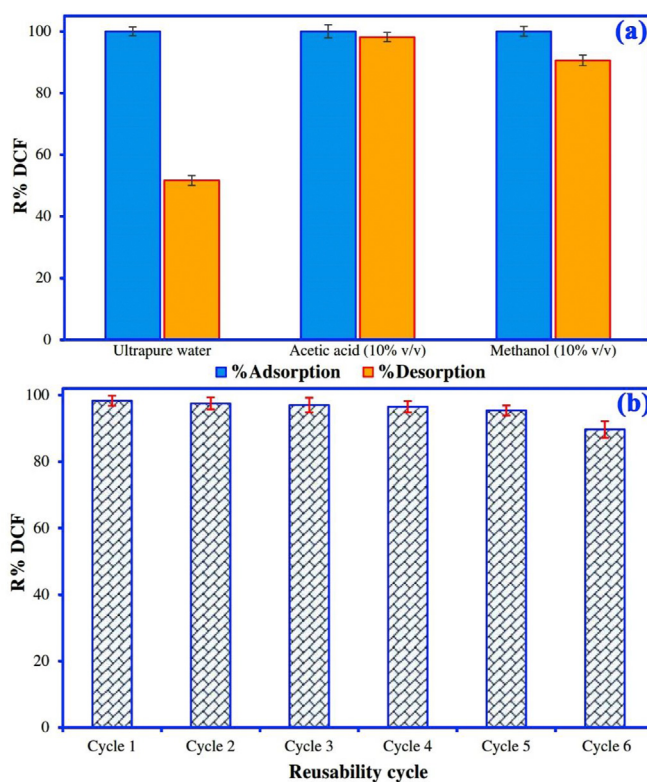


Fig. 8. (a) Adsorption and desorption of magnetic GO/ZIF-8/γ-AIOOH-NC using three eluents and (b) efficiency of magnetic GO/ZIF-8/γ-AIOOH-NC for DCF adsorption in the cycles using acetic acid (10% v/v) as eluent.

in the desorption of DCF from the nanocomposite. The low capability of ultrapure water for the desorption of DCF from the nanocomposite indicates that most of the DCF removal was probably by chemisorption. Also, the effectiveness of acetic acid can be due to the emerged repulsion between the adsorbent and the DCF molecules are due to the increase in the number of positively charged sites at the adsorbent surface under acidic conditions (Arabkhani et al., 2020). Although methanol solution also showed high desorption efficiency of >95%, acetic acid is safer to handle and to scale up than methanol. Thus, the recyclability of the adsorbent was further tested in six cycles of adsorption-desorption by acetic acid (10% v/v). As illustrated in Fig. 8b, the nanocomposite capacity was

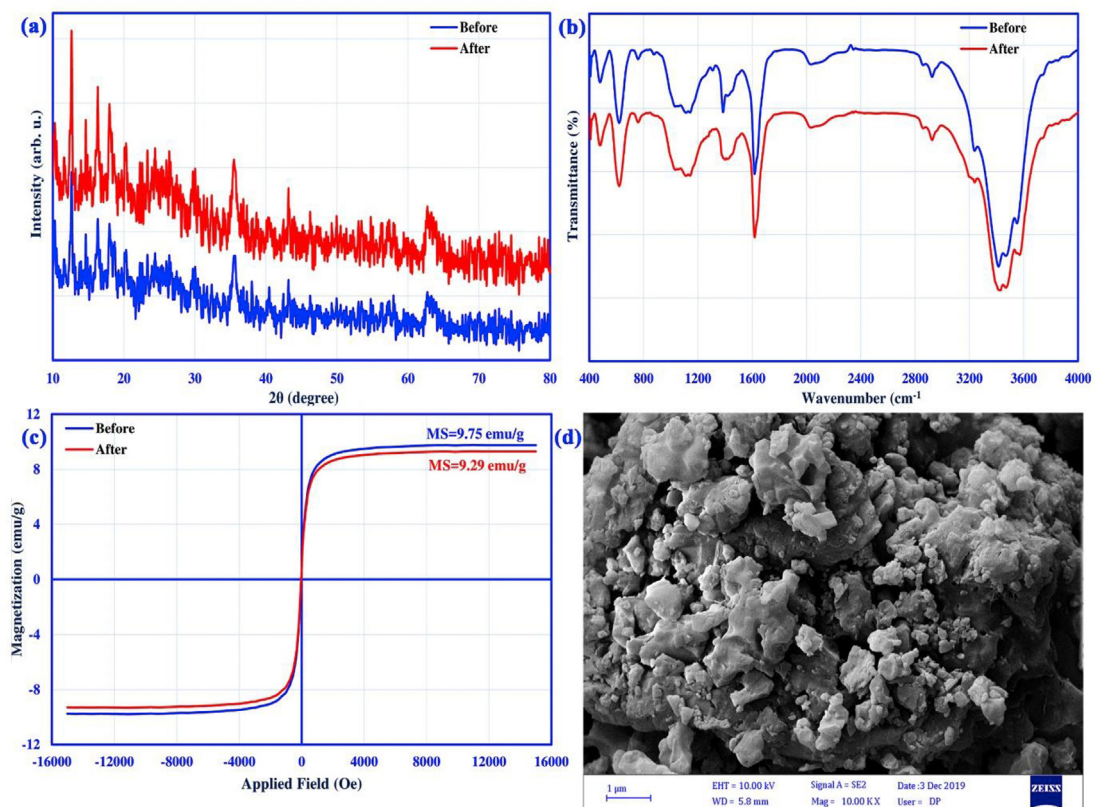


Fig. 9. (a) XRD patterns, (b) FT-IR spectra, and (c) VSM of magnetic GO/ZIF-8/ γ -AlOOH-NC before and after the fifth cycle, and (d) FE-SEM image of magnetic GO/ZIF-8/ γ -AlOOH-NC after the fifth cycle.

maintained even after five consecutive cycles, which indicates the complete desorption of DCF by acetic acid (10% v/v) and stability of adsorbent during the reusability tests. From the reusability results, it can be concluded that the nanocomposite possesses a very good stability and can be used several times in the adsorption process of DCF.

Furthermore, the XRD pattern (Fig. 9a), FT-IR spectrum (Fig. 9b), VSM (Fig. 9c), and FE-SEM image (Fig. 9d) of the nanocomposite after five cycles of DCF adsorption are the same as those obtained before adsorption, which re-emphasize the nanocomposite stability and indicate insignificant changes in the nanocomposite structure and morphology. This phenomenon suggests that the nanoparticles are strongly bonded to the surface of GO nanosheets, resulting in nanocomposite stability during the adsorption-desorption cycles. In addition, the magnetic stability of the nanocomposite was also investigated after using in five adsorption-desorption cycles, and the saturation magnetization of the nanocomposite before and after DCF adsorption was compared. Fig. 9c depicts that the nanocomposite saturation magnetization slightly decreases (from 9.75 to 9.29 emu g⁻¹) after reusability test. Therefore, the nanocomposite can be considered as a reliable candidate for the magnetic separation of DCF without producing a secondary pollution.

3.7. Proposed adsorption mechanisms

The results obtained from the FT-IR analysis, isotherm, kinetic, thermodynamic, and desorption studies were applied for the investigation of possible adsorption mechanisms. According to FTIR analysis of before and after the adsorption process (Fig. 10), after the DCF adsorption on nanocomposite, the appearance of new

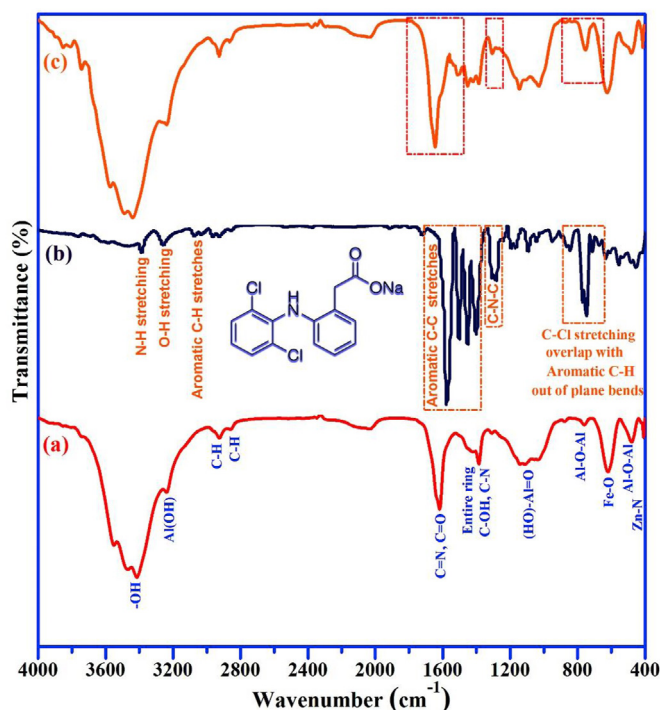


Fig. 10. FT-IR spectra of (a) magnetic GO/ZIF-8/ γ -AlOOH-NC before adsorption of DCF, (b) DCF, and (c) magnetic GO/ZIF-8/ γ -AlOOH-NC after adsorption of DCF.

characteristic peaks related to DCF molecules in nanocomposite spectra suggested that the adsorption process involved chemical interaction. Also, the better fit of the adsorption kinetics with the pseudo-second-order model, as well as higher enthalpy of adsorption ($\Delta H^\circ > 40 \text{ kJ mol}^{-1}$) reinforce this fact. On the other hand, according to the regeneration result, the weak desorption efficiency of DCF in ultrapure water (51.7%) relative to methanol (90.6%), and acetic acid (98.2%) indicate that the chemisorption may have been the major mode of adsorption mechanism which is in line with other results (Arabkhani et al., 2020). However, the value of E factor obtained from D-R isotherm model (2.61 kJ mol^{-1}) suggests that the possibility of physical adsorption together with the chemisorption process cannot be avoided. According to the nanocomposite and DCF structures, the adsorption mechanism can be included a combination of different mechanisms such as H-bonding, electrostatic attraction, n- π interactions, π - π interactions, and physical adsorption. As long as adsorption occurs in the aqueous environments, water molecules are in contact with adsorbent surface, and surface oxygen groups are as ideal sites for water molecules for the formation of hydrogen-bonding that compete with organic compounds for occupying the adsorption sites. This could block the sites of adsorption and reduce the accessibility and affinity of adsorbate, causing a reduction in the adsorption capacity. Therefore, hydrogen-bonding could not be considered as a major adsorption mechanism. On the other hand, the significant effect of pH on DCF adsorption (bases on the pK_a value of DCF and pH_{zpc} of the nanocomposite) showed that electrostatic attraction plays a highly remarkable role in DCF adsorption. Another mechanism including π - π interactions is proposed for the explanation of DCF bonding with the nanocomposite. The interactions of π - π can take place between the aromatic rings (in

GO nanosheets) and aromatic moieties (in DCF molecules) through π electron donors and π electron acceptors that can be confirmed by the comparison of the nanocomposite FT-IR spectra before and after DCF adsorption based on the shift occurred for the aromatic C=C bonds from 1322 to 1311 cm^{-1} . The schematic of the possible adsorption mechanisms of DCF molecules by nanocomposite is shown in Fig. 11. EDX analysis was carried out to approve DCF adsorption onto the nanocomposite. As can be seen in Fig. 12, the EDX spectrum of the nanocomposite shows sodium and chlorine elements attributed to DCF adsorbed onto the adsorbent surface (Fig. 12a) that confirm the adsorption of DCF. In addition, Fig. 12b shows the distribution of nanocomposite elements after DCF adsorption. The EDX mapping clearly shows the presence of sodium and chlorine elements along with the elements of the nanocomposite and indicates DCF adsorption onto whole surface of the nanocomposite.

3.8. Practical application of magnetic GO/ZIF-8/ γ -AlOOH-NC for the simulated hospital effluents

Real wastewater effluents contains several organic and inorganic constituents in addition to the pharmaceutical compounds (Ateia et al., 2017b). Therefore, the performance of magnetic GO/ZIF-8/ γ -AlOOH-NC was tested in a simulated hospital effluent. The detailed compositions and concentrations of each constituent were given in Table S7. The simulated effluent treatment was evaluated by UV-vis spectra (190–500 nm) before and after adsorption and its efficiency was calculated by monitoring the areas under the absorption bands (Fig. S6). The average removal percentage of the DCF from simulated hospital effluent was 95.29% (Table S8), which is in agreement with the maximum removal percentage (99.29%)

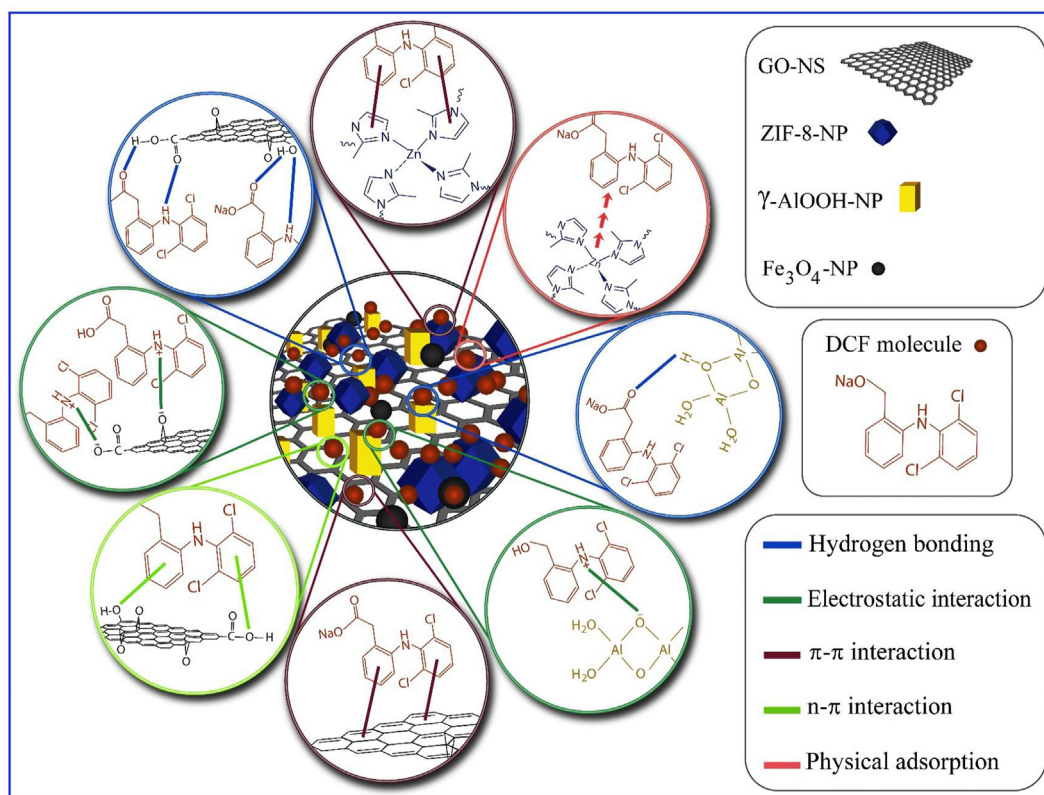


Fig. 11. Possible adsorption mechanisms of DCF molecules by magnetic GO/ZIF-8/ γ -AlOOH-NC.

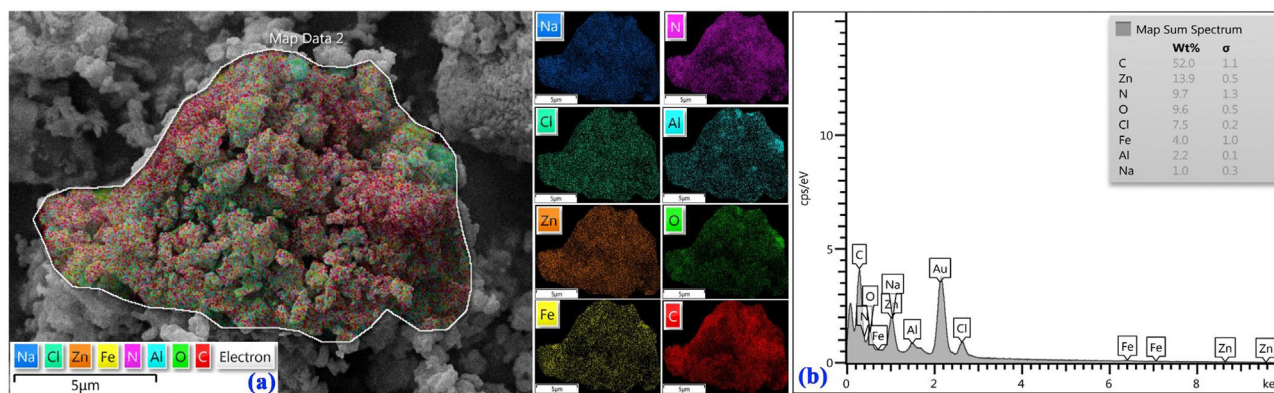


Fig. 12. (a) EDX mapping and (b) EDX analysis of magnetic GO/ZIF-8/ γ -AIOOH-NC after DCF adsorption.

presented in reported optimal conditions. Accordingly, the nanocomposite is a promising and efficient adsorbent for treating real hospital effluents.

4. Conclusions and future recommendations

In this study, a novel magnetic adsorbent with ultra-high adsorption capacity towards diclofenac was synthesized via the decoration of GO nanosheets with ZIF-8, Fe₃O₄ and γ -AIOOH nanoparticles. The saturation magnetization and BET surface area for magnetic GO/ZIF-8/ γ -AIOOH-NC were 9.75 emu g⁻¹ and 777 m² g⁻¹, respectively. This new adsorbent was tested to thoroughly elucidate the impacts of the operation parameters, including contact time, adsorbent mass, initial solution pH, temperature, initial DCF concentration, and their interactions on the removal of DCF. The optimum conditions were predicted by RSM-CCD, which were found to be 2 mg of magnetic GO/ZIF-8/ γ -AIOOH-NC, a contact time of 50 min, temperature of 30 °C, pH of 7.5, and initial DCF concentration of 80 mg g⁻¹. Langmuir model was appropriate to fit the equilibrium data, and the maximum capacity of magnetic GO/ZIF-8/ γ -AIOOH-NC at saturation condition was 2594 mg g⁻¹, which was higher than all adsorbents reported previously. This significant improvement was attributed to the high surface area and abundance of accessible adsorption sites in the mesoporous region. The reusability tests revealed that the synthesized magnetic nanocomposite could be favorably reusable for at least five consecutive cycles. In addition, the nanocomposite was used successfully to treat the simulated hospital effluents. Future studies should expand the testing of this promising magnetic adsorbent for other classes of emerging contaminants with different molecular size, charge, and polarity.

Author contribution statement

Mr. Payam Arabkhani: Conceptualization, Investigation, Formal analysis, Writing - original draft, Writing - review & editing, Data curation; Validation.

Dr. Hamedreza Javadian: Supervision, Conceptualization, Writing - review & editing, Methodology; Data curation; Validation.

Dr. Arash Asfaram: Supervision, Conceptualization, Writing - review & editing, Methodology; Data curation; Validation.

Dr. Mohamed Ateia: Supervision; Conceptualization; Writing - review & editing.

Declaration of competing interest

The authors declare that they have no known competing financial interests or personal relationships that could have appeared to influence the work reported in this paper.

Appendix A. Supplementary data

Supplementary data to this article can be found online at <https://doi.org/10.1016/j.chemosphere.2021.129610>.

References

- Abdi, J., Mahmoodi, N.M., Vossoughi, M., Alemzadeh, I., 2019. Synthesis of magnetic metal-organic framework nanocomposite (ZIF-8@ SiO₂@ MnFe₂O₄) as a novel adsorbent for selective dye removal from multicomponent systems. *Microporous Mesoporous Mater.* 273, 177–188.
- Abdollahifar, M., Hidaryan, M., Jafari, P., 2018. The role anions on the synthesis of AIOOH nanoparticles using simple solvothermal method. *Bol. Soc. Espanola Ceram. Vidr.* 57, 66–72.
- Accocella, M.R., De Pascale, M., Maggio, M., Guerra, G., 2015. Graphite oxide as catalyst for diastereoselective Mukaiyama aldol reaction of 2-(trimethylsilyloxy)furan in solvent free conditions. *J. Mol. Catal. Chem.* 408, 237–241.
- Aksakal, O., Ucun, H., 2010. Equilibrium, kinetic and thermodynamic studies of the biosorption of textile dye (Reactive Red 195) onto *Pinus sylvestris* L. *J. Hazard Mater.* 181, 666–672.
- Alam, S.N., Sharma, N., Kumar, L., 2017. Synthesis of graphene oxide (GO) by modified hummers method and its thermal reduction to obtain reduced graphene oxide (rGO). *Graphene* 6, 1–18.
- Andrew Lin, K.-Y., Yang, H., Lee, W.-D., 2015. Enhanced removal of diclofenac from water using a zeolitic imidazole framework functionalized with cetyltrimethylammonium bromide (CTAB). *RSC Adv.* 5, 81330–81340.
- Arabkhani, P., Asfaram, A., 2020. Development of a novel three-dimensional magnetic polymer aerogel as an efficient adsorbent for malachite green removal. *J. Hazard Mater.* 384, 121394.
- Arabkhani, P., Asfaram, A., Ateia, M., 2020. Easy-to-prepare graphene oxide/sodium montmorillonite polymer nanocomposite with enhanced adsorption performance. *J. Water Process Eng.* 38, 101651.
- Asfaram, A., Dil, E.A., Arabkhani, P., Sadeghfar, F., Ghaedi, M., 2020. Magnetic Cu: CuO-GO nanocomposite for efficient dispersive micro-solid phase extraction of polycyclic aromatic hydrocarbons from vegetable, fruit, and environmental water samples by liquid chromatographic determination. *Talanta* 218, 121131.
- Ateia, M., Koch, C., Jelavić, S., Hirt, A., Quinson, J., Yoshimura, C., Johnson, M., 2017a. Green and facile approach for enhancing the inherent magnetic properties of carbon nanotubes for water treatment applications. *PLoS One* 12 (7), e0180636.
- Ateia, M., Apul, O.G., Shimizu, Y., Muflihah, A., Yoshimura, C., Karanfil, T., 2017b. Elucidating adsorptive fractions of natural organic matter on carbon nanotubes. *Environ. Sci. Technol.* 51 (12), 7101–7110.
- Ateia, M., Attia, M.F., Maroli, A., Tharayil, N., Alexis, F., Whitehead, D.C., Karanfil, T., 2018. Rapid removal of poly-and perfluorinated alkyl substances by poly(ethylenimine)-functionalized cellulose microcrystals at environmentally relevant conditions. *Environ. Sci. Technol. Lett.* 5 (12), 764–769.
- Ateia, M., Helbling, D.E., Dichtel, W.R., 2020. Best practices for evaluating new materials as adsorbents for water treatment. *ACS Mater. Lett.* 2 (11), 1532–1544.
- Basith, N.M., Raj, R.A., AlSalhi, M.S., Devanesan, S., Askar Ali, S.J., Rajasekar, S., Sundaram, R., Ragupathi, C., 2016. Structural, magnetic, optical, and Catalytic properties of Fe₃O₄ nanoparticles by the sol-gel method. *J. Supercond. Nov.*

- Magnetism 29, 2053–2058.
- Bhadra, B.N., Ahmed, I., Kim, S., Jhung, S.H., 2017. Adsorptive removal of ibuprofen and diclofenac from water using metal-organic framework-derived porous carbon. *Chem. Eng. J.* 314, 50–58.
- Bhadra, B.N., Seo, P.W., Jhung, S.H., 2016. Adsorption of diclofenac sodium from water using oxidized activated carbon. *Chem. Eng. J.* 301, 27–34.
- Bohström, Z., Lillerud, K.P., 2018. Preparation of chabazite with mesopores templated from a cationic polymer. *Microporous Mesoporous Mater.* 271, 295–300.
- Boruah, P.K., Das, M.R., 2020. Dual responsive magnetic Fe₃O₄-TiO₂/graphene nanocomposite as an artificial nanozyme for the colorimetric detection and photodegradation of pesticide in an aqueous medium. *J. Hazard Mater.* 385, 121516.
- Choi, E., Song, K., An, S., Lee, K., Youn, M., Park, K., Jeong, S., Kim, H., 2018. Cu/ZnO/AlOOH catalyst for methanol synthesis through CO₂ hydrogenation. *Kor. J. Chem. Eng.* 35, 73–81.
- Cychoz, K.A., Guillet-Nicolas, R., García-Martínez, J., Thommes, M., 2017. Recent advances in the textural characterization of hierarchically structured nanoporous materials. *Chem. Soc. Rev.* 46, 389–414.
- Dubinín, M., Serpinsky, V., 1981. Isotherm equation for water vapor adsorption by microporous carbonaceous adsorbents. *Carbon* 19, 402–403.
- El-Maghrabi, H.H., Abdelmaged, S.M., Nada, A.A., Zahran, F., El-Wahab, S.A., Yahea, D., Hussein, G.M., Atrees, M.S., 2017. Magnetic graphene based nanocomposite for uranium scavenging. *J. Hazard Mater.* 322, 370–379.
- Fan, L., Lu, Y., Yang, L.-Y., Huang, F., Ouyang, X.-k., 2019. Fabrication of polyethylenimine-functionalized sodium alginate/cellulose nanocrystal/polyvinyl alcohol core-shell microspheres ((PVA/SA/CNC)@PEI) for diclofenac sodium adsorption. *J. Colloid Interface Sci.* 554, 48–58.
- Feng, Y., Li, Y., Xu, M., Liu, S., Yao, J., 2016. Fast adsorption of methyl blue on zeolitic imidazolate framework-8 and its adsorption mechanism. *RSC Adv.* 6, 109608–109612.
- Ghaedi, M., Rozkkoosh, Z., Asfaram, A., Mirtamizdoust, B., Mahmoudi, Z., Bazrafshan, A.A., 2015. Comparative studies on removal of Erythrosine using ZnS and AgOH nanoparticles loaded on activated carbon as adsorbents: kinetic and isotherm studies of adsorption. *Spectrochim. Acta Mol. Biomol. Spectrosc.* 138, 176–186.
- Ghorbani-Choghamarani, A., Hajjami, M., Tahmasbi, B., Noori, N., 2016. Boehmite silica sulfuric acid: as a new acidic material and reusable heterogeneous nanocatalyst for the various organic oxidation reactions. *J. Iran. Chem. Soc.* 13, 2193–2202.
- Habibi, N., 2014. Preparation of biocompatible magnetite-carboxymethyl cellulose nanocomposite: characterization of nanocomposite by FTIR, XRD, FESEM and TEM. *Spectrochim. Acta Mol. Biomol. Spectrosc.* 131, 55–58.
- Hasan, Z., Khan, N.A., Jhung, S.H., 2016. Adsorptive removal of diclofenac sodium from water with Zr-based metal-organic frameworks. *Chem. Eng. J.* 284, 1406–1413.
- Heu, R., Ateia, M., Awfa, D., Punyapalaku, P., Yoshimura, C., 2020. Photocatalytic degradation of organic micropollutants in water by Zr-MOF/GO composites. *J. Compo. Sci.* 4 (2), 54.
- Hiew, B.Y.Z., Lee, L.Y., Lai, K.C., Gan, S., Thangalazhy-Gopakumar, S., Pan, G.-T., Yang, T.C.-K., 2019a. Adsorptive decontamination of diclofenac by three-dimensional graphene-based adsorbent: response surface methodology, adsorption equilibrium, kinetic and thermodynamic studies. *Environ. Res.* 168, 241–253.
- Hiew, B.Y.Z., Lee, L.Y., Lee, X.J., Gan, S., Thangalazhy-Gopakumar, S., Lim, S.S., Pan, G.-T., Yang, T.C.-K., 2019b. Adsorptive removal of diclofenac by graphene oxide: optimization, equilibrium, kinetic and thermodynamic studies. *J. Taiwan Inst. Chem. Eng.* 98, 150–162.
- Ho, Y.-S., 2006. Review of second-order models for adsorption systems. *J. Hazard Mater.* 136, 681–689.
- Hu, D., Huang, H., Jiang, R., Wang, N., Xu, H., Wang, Y.-G., Ouyang, X.-k., 2019. Adsorption of diclofenac sodium on bilayer amino-functionalized cellulose nanocrystals/chitosan composite. *J. Hazard Mater.* 369, 483–493.
- Huang, L., Mao, N., Yan, Q., Zhang, D., Shuai, Q., 2019. Magnetic covalent organic frameworks for the removal of diclofenac sodium from water. *ACS Appl. Nano Mater.* 3, 319–326.
- Jabbari, V., Veleta, J., Zarei-Chaleshtori, M., Gardea-Torresdey, J., Villagrán, D., 2016a. Green synthesis of magnetic MOF@GO and MOF@CNT hybrid nanocomposites with high adsorption capacity towards organic pollutants. *Chem. Eng. J.* 304, 774–783.
- Jabbari, V., Veleta, J.M., Zarei-Chaleshtori, M., Gardea-Torresdey, J., Villagrán, D., 2016b. Green synthesis of magnetic MOF@GO and MOF@CNT hybrid nanocomposites with high adsorption capacity towards organic pollutants. *Chem. Eng. J.* 304, 774–783.
- Jauris, I.M., Matos, C.F., Saucier, C., Lima, E.C., Zarbin, A.J.G., Fagan, S.B., Machado, F.M., Zanella, I., 2016. Adsorption of sodium diclofenac on graphene: a combined experimental and theoretical study. *Phys. Chem. Chem. Phys.* 18, 1526–1536.
- Jian, M., Liu, B., Zhang, G., Liu, R., Zhang, X., 2015. Adsorptive removal of arsenic from aqueous solution by zeolitic imidazolate framework-8 (ZIF-8) nanoparticles. *Colloid. Surface. Physicochem. Eng. Aspect.* 465, 67–76.
- Kaur, H., Mohanta, G.C., Gupta, V., Kukkar, D., Tyagi, S., 2017. Synthesis and characterization of ZIF-8 nanoparticles for controlled release of 6-mercaptopurine drug. *J. Drug Deliv. Sci. Technol.* 41, 106–112.
- Kaur, N., Kaur, M., Singh, D., 2019. Fabrication of mesoporous nanocomposite of graphene oxide with magnesium ferrite for efficient sequestration of Ni (II) and Pb (II) ions: adsorption, thermodynamic and kinetic studies. *Environ. Pollut.* 253, 111–119.
- Khafri, H.Z., Ghaedi, M., Asfaram, A., Safarpour, M., 2017. Synthesis and characterization of ZnS:Ni-NPs loaded on AC derived from apple tree wood and their applicability for the ultrasound assisted comparative adsorption of cationic dyes based on the experimental design. *Ultrason. Sonochem.* 38, 371–380.
- Khalid, A., Rowles, L.S., Xiao, M., Ramirez-Sanchez, I., Bello, D., Karanfil, T., Saleh, N.B., Apul, O.G., 2020. Mesoporous activated carbon shows superior adsorption affinity for 11-nor-9-carboxy-Δ⁹-tetrahydrocannabinol in water. *npj Clean Water* 3 (1), 1–5.
- Kida, K., Okita, M., Fujita, K., Tanaka, S., Miyake, Y., 2013. Formation of high crystalline ZIF-8 in an aqueous solution. *CrystEngComm* 15, 1794–1801.
- Kim, S.-M., Lee, Y.-J., Jun, K.-W., Park, J.-Y., Potdar, H., 2007. Synthesis of thermostable high surface area alumina powder from sol-gel derived boehmite. *Mater. Chem. Phys.* 104, 56–61.
- Krajišnik, D., Daković, A., Milojević, M., Malenović, A., Kragović, M., Bogdanović, D.B., Dondur, V., Milić, J., 2011. Properties of diclofenac sodium sorption onto natural zeolite modified with cetylpyridinium chloride. *Colloids Surf. B Biointerfaces* 83, 165–172.
- Kunde, G.B., Sehgal, B., Ganguli, A.K., 2019. Synthesis of mesoporous rebar MWCNT/alumina composite (RMAC) nodules for the effective removal of methylene blue and Cr (VI) from an aqueous medium. *J. Hazard Mater.* 374, 140–151.
- Langmuir, I., 1918. The adsorption of gases on plane surfaces of glass, mica and platinum. *J. Am. Chem. Soc.* 40, 1361–1403.
- LeVan, M.D., Vermeulen, T., 1981. Binary Langmuir and Freundlich isotherms for ideal adsorbed solutions. *J. Phys. Chem.* 85, 3247–3250.
- Li, M.-f., Liu, Y.-g., Liu, S.-b., Zeng, G.-m., Hu, X.-j., Tan, X.-f., Jiang, L.-h., Liu, N., Wen, J., Liu, X.-h., 2018. Performance of magnetic graphene oxide/diethylene-triaminepentaacetic acid nanocomposite for the tetracycline and ciprofloxacin adsorption in single and binary systems. *J. Colloid Interface Sci.* 521, 150–159.
- Liang, X.X., Omer, A.M., Hu, Z.-h., Wang, Y.g., Yu, D., Ouyang, X.-k., 2019. Efficient adsorption of diclofenac sodium from aqueous solutions using magnetic amine-functionalized chitosan. *Chemosphere* 217, 270–278.
- Liu, X., Chen, X., Ma, H.-A., Jia, X., Wu, J., Yu, T., Wang, Y., Guo, J., Petitgirard, S., Bina, C.R., 2016. Ultrahard stitching of nanotwinned diamond and cubic boron nitride in C 2-BN composite. *Sci. Rep.* 6, 30518.
- Lu, W., Li, J., Sheng, Y., Zhang, X., You, J., Chen, L., 2017. One-pot synthesis of magnetic iron oxide nanoparticle-multiwalled carbon nanotube composites for enhanced removal of Cr(VI) from aqueous solution. *J. Colloid Interface Sci.* 505, 1134–1146.
- Lu, W., Shen, Y., Xie, A., Zhang, W., 2010. Green synthesis and characterization of superparamagnetic Fe₃O₄ nanoparticles. *J. Magn. Magn. Mater.* 322, 1828–1833.
- Mahmoudi, M., Akhavan, O., Ghavami, M., Rezaee, F., Ghiasi, S.M.A., 2012. Graphene oxide strongly inhibits amyloid beta fibrillation. *Nanoscale* 4, 7322–7325.
- Mousa, H.M., Alfadhel, H., Ateia, M., Gomaa, A.A., Abdel-Jaber, G.T., 2020. Poly-sulfone-iron acetate/polyamide nanocomposite membrane for oil-water separation. *Environ. Nanotechnol. Monit. Manag.* 100314.
- Muzyka, R., Kwoka, M., Smędowski, Ł., Diez, N., Gryglewicz, G., 2017. Oxidation of graphite by different modified Hummers methods. *N. Carbon Mater.* 32, 15–20.
- Nam, S.-W., Jung, C., Li, H., Yu, M., Flora, J.R.V., Boateng, L.K., Her, N., Zoh, K.-D., Yoon, Y., 2015. Adsorption characteristics of diclofenac and sulfamethoxazole to graphene oxide in aqueous solution. *Chemosphere* 136, 20–26.
- Saini, J., Garg, V., Gupta, R., 2018. Removal of Methylene Blue from aqueous solution by Fe₃O₄@Ag/SiO₂ nanospheres: synthesis, characterization and adsorption performance. *J. Mol. Liq.* 250, 413–422.
- Schejv, A., Balan, L., Falk, V., Aranda, L., Medjahdi, G., Schneider, R., 2014. Controlling ZIF-8 nano- and microcrystal formation and reactivity through zinc salt variations. *CrystEngComm* 16, 4493–4500.
- Shi, H., Chen, X., Liu, K., Ding, X., Liu, W., Xu, M., 2020. Heterogeneous Fenton ferrous oxide-reduced graphene oxide-based composite microjets for efficient organic dye degradation. *J. Colloid Interface Sci.* 572, 39–47.
- Singha, B., Das, S.K., 2013. Adsorptive removal of Cu (II) from aqueous solution and industrial effluent using natural/agricultural wastes. *Colloids Surf. B Biointerfaces* 107, 97–106.
- Tanaka, S., Miyashita, R., 2017. Aqueous-system-enabled spray-drying technique for the synthesis of hollow polycrystalline ZIF-8 MOF particles. *ACS Omega* 2, 6437–6445.
- Wang, H., Zhou, Y., Guo, Y., Liu, W., Dong, C., Wu, Y., Li, S., Shuang, S., 2012. β-Cyclodextrin/Fe₃O₄ hybrid magnetic nano-composite modified glassy carbon electrode for tryptophan sensing. *Sensor. Actuator. B Chem.* 163, 171–178.
- Wawrzkiwicz, M., Hubicki, Z., 2009. Equilibrium and kinetic studies on the adsorption of acidic dye by the gel anion exchanger. *J. Hazard Mater.* 172, 868–874.
- Weber, W.J., Morris, J.C., 1963. Kinetics of adsorption on carbon from solution. *J. Sanit. Eng. Div.* 89, 31–60.
- Wong, Y., Szeto, Y., Cheung, W., McKay, G., 2004. Pseudo-first-order kinetic studies of the sorption of acid dyes onto chitosan. *J. Appl. Polym. Sci.* 92, 1633–1645.
- Wu, L., Du, C., He, J., Yang, Z., Li, H., 2020. Effective adsorption of diclofenac sodium from neutral aqueous solution by low-cost lignite activated cokes. *J. Hazard Mater.* 384, 121284.
- Xie, W., Huang, M., 2018. Immobilization of *Candida rugosa* lipase onto graphene oxide Fe₃O₄ nanocomposite: characterization and application for biodiesel production. *Energy Convers. Manag.* 159, 42–53.
- Xiong, T., Yuan, X., Wang, H., Wu, Z., Jiang, L., Leng, L., Xi, K., Cao, X., Zeng, G., 2019. Highly efficient removal of diclofenac sodium from medical wastewater by Mg/

- Al layered double hydroxide-poly(m-phenylenediamine) composite. *Chem. Eng. J.* 366, 83–91.
- Yang, K., Yan, Y., Wang, H., Sun, Z., Chen, W., Kang, H., Han, Y., Zahng, W., Sun, X., Li, Z., 2018. Monodisperse Cu/Cu₂O@C core-shell nanocomposite supported on rGO layers as an efficient catalyst derived from a Cu-based MOF/GO structure. *Nanoscale* 10, 17647–17655.
- Yang, Y., Yu, W., He, S., Yu, S., Chen, Y., Lu, L., Shu, Z., Cui, H., Zhang, Y., Jin, H., 2019. Rapid adsorption of cationic dye-methylene blue on the modified montmorillonite/graphene oxide composites. *Appl. Clay Sci.* 168, 304–311.
- Yu, F., Sun, S., Ma, J., Han, S., 2015. Enhanced removal performance of arsenate and arsenite by magnetic graphene oxide with high iron oxide loading. *Phys. Chem. Chem. Phys.* 17, 4388–4397.
- Zhang, H., Li, P., Cui, W., Liu, C., Wang, S., Zheng, S., Zhang, Y., 2016. Synthesis of nanostructured γ -AlOOH and its accelerating behavior on the thermal decomposition of AP. *RSC Adv.* 6, 27235–27241.
- Zhang, S., Shao, Y., Liao, H., Engelhard, M.H., Yin, G., Lin, Y., 2011. Polyelectrolyte-induced reduction of exfoliated graphite oxide: a facile route to synthesis of soluble graphene nanosheets. *ACS Nano* 5, 1785–1791.
- Zheng, J., Cheng, C., Fang, W.-J., Chen, C., Yan, R.-W., Huai, H.-X., Wang, C.-C., 2014. Surfactant-free synthesis of a Fe₃O₄@ ZIF-8 core-shell heterostructure for adsorption of methylene blue. *CrystEngComm* 16, 3960–3964.
- Zheng, X., Wang, J., Xue, X., Liu, W., Kong, Y., Cheng, R., Yuan, D., 2018. Facile synthesis of Fe₃O₄@MOF-100(Fe) magnetic microspheres for the adsorption of diclofenac sodium in aqueous solution. *Environ. Sci. Pollut. Control Ser.* 25, 31705–31717.